Medical Engineering and Physics 131 (2024) 104229

Contents lists available at ScienceDirect

Medical Engineering and Physics

journal homepage: www.elsevier.com/locate/medengphy

Paper

Towards a reduced order model for EVAR planning and intra-operative navigation

Monica Emendi [a,*,1], Eirini Kardampiki [a,b,1], Karen-Helene Støverud [b], Antonio Martinez Pascual [a], Leonardo Geronzi [a], Sigrid Kaarstad Dahl [b], Victorien Prot [c], Paal Skjetne [d], Marco Evangelos Biancolini [a]

[a] Department of Enterprise Engineering, University of Rome Tor Vergata, Via del Politecnico 1, Rome, 00133, Italy
[b] SINTEF Digital, Professor Brochs Gate 2, Trondheim, 7030, Norway
[c] Department of Structural Engineering, The Norwegian University of Science and Technology, Richard Birkelands vei 1A, Trondheim, 7034, Norway
[d] SINTEF Industry, S.P. Andersensvei 15B, Trondheim, 7030, Norway

ARTICLE INFO

Keywords:
Reduced order model
Endovascular aneurysm repair
Abdominal aortic aneurysm
Finite element analysis
Mesh morphing

ABSTRACT

Introduction: The pre-operative planning and intra-operative navigation of the endovascular aneurysm repair (EVAR) procedure are currently challenged by the aortic deformations that occur due to the insertion of a stiff guidewire. Hence, a fast and accurate predictive tool may help clinicians in the decision-making process and during surgical navigation, potentially reducing the radiations and contrast dose. To this aim, we generated a reduced order model (ROM) trained on parametric finite element simulations of the aortic wall-guidewire interaction.

Method: A Design of Experiments (DOE) consisting of 300 scenarios was created spanning over seven parameters. Radial basis functions were used to achieve a morphological parametrization of the aortic geometry. The ROM was built using 200 scenarios for training and the remaining 100 for validation.

Results: The developed ROM estimated the displacement of aortic nodes with a relative error below 5.5% for all the considered validation cases. From a preliminary analysis, the aortic elasticity, the stiffness of the guidewire and the tortuosity of the cannulated iliac artery proved to be the most influential parameters.

Conclusions: Once built, the ROM provided almost real-time and accurate estimations of the guidewire-induced aortic displacement field, thus potentially being a promising pre- and intra-operative tool for clinicians.

1. Introduction

Endovascular aneurysm repair (EVAR) is a minimally invasive procedure for the treatment of abdominal aortic aneurysms. During EVAR, the insertion of endovascular devices causes deformations to the aortoiliac structure [1].

Accurate pre-operative planning is crucial to assess the feasibility of the guidewire navigation and stent-graft delivery. Appropriate size and placement of the stent-graft is necessary to minimize the chance of procedural failure and post-operative complications such as endoleaks, endograft migration, or collapse and kinking of the endograft limbs. According to Daye and Walker [2], the rate of EVAR complications ranges between 16% and 30% with a re-intervention rate of 19% of the treated patients. High tortuosity of the iliac arteries and an increased level of calcifications are associated with a severe risk of procedure failure, which in the worst cases leads to revision surgeries [3,4]. According to the EUROSTAR registry study [5], 13% of infrarenal EVAR patients had access problems due to stenosis, excessive tortuosity, or narrow iliac arteries. Previous works [6–8] remarked that the deformation caused by the insertion of the stiff guidewire affects the final configuration of the vessel. Nevertheless, this updated vessel morphology is not considered during the pre-operative planning, leading to potential sub-optimal stent-graft sizing [9]. Moreover, the incidence of deficient stent-graft selection is particularly high in cases of iliac arteries stenting and tortuous vessels [7]. Therefore, the prediction of the deformed aortic configuration after the insertion of the guidewire could be of added value for pre-

* Corresponding author.
E-mail address: monica.emendi@alumni.uniroma2.eu (M. Emendi).
[1] Emendi and Kardampiki have contributed equally and are therefore both first authors.

https://doi.org/10.1016/j.medengphy.2024.104229
Received 12 September 2023; Received in revised form 6 August 2024; Accepted 13 August 2024
Available online 16 August 2024

operative planning, which currently relies on Computed Tomography (CT) scans solely. The interaction between the aorta and the guidewire has been successfully modeled with finite element analysis (FEA) in previous studies [10–12]. For example, as shown by Daoudal et al. [13], the simulation of guidewire-induced deformations allows to predict an accidental coverage of the internal iliac artery. Moreover, Dupont et al. [8] presented a numerical method that simulated a FEVAR (Fenestrated EVAR) procedure, able to predict the position of the renal ostia after the tools' insertion, aiming at reducing intra- and post-operative complications such as catheterization difficulties and incorrect perfusion of the renal and visceral arteries.

Intra-operative navigation during EVAR is currently mainly performed through 2D fluoroscopy and Digital Subtraction Angiography (DSA) for real-time visualization of the inserted tools and vessel morphology. These acquisitions entail the use of radiations and contrast agents, whose dose increases along with the complexity of the case, resulting in potentially harmful exposure for both patient and clinicians [14]. Furthermore, the limited 2D view provided by the above-mentioned imaging techniques could increase the operation time and make the intra-operative visualization poor [15]. For this purpose, imaging fusion techniques, that combine the pre-operative CT and X-ray acquisitions are currently adopted. Still, the registration between pre- and intra-operative data can be low in accuracy and may demand manual adjustments due to the guidewire-induced deformations in the aortic configuration [16,17]. Thus, predictive intra-operative aortic displacements obtained from finite element analysis could be helpful for navigation purposes, allowing to reduce the amount of radiation and contrast agent.

The current limitation for high-fidelity simulations remains the relatively high computational cost and the clinical exploitability. To this aim, Reduced Order Models (ROMs) [18,19] could be a valuable computational tool that can offer a new perspective on the clinicians' decision-making process, compatible with the limited time frame in the clinic. In the past, ROMs have been used as an alternative to solve full order computational problems mainly in classical mechanics. Nowadays, the ROM approach is also spreading in the clinical research, aiming to support the diagnosis [20], planning [21,22], and intra-operative procedure [23,24]. Nevertheless, the ROM build-up of cardiovascular problems is still challenging, mainly due to their non-linear behavior, multi-scale nature and patients' morphological diversity [25]. Regarding the morphological variation, a baseline patient specific geometry can be morphed toward a desired configuration with Radial Basis Functions (RBF) [26–28] rapidly and precisely, avoiding the Computer Aided Design (CAD) reconstruction.

Taking this into consideration, our study proposes the generation of a pre- and intra-operative interactive environment to predict the guidewire-induced aortic deformation as a function of seven critical mechanical, morphological and clinical parameters. The development of such a pipeline can contribute to substantially reduce the computational expense, compared to high-fidelity simulations, while ensuring accurate results.

To the best of our knowledge, this study is the first of its kind that proposes a reduced order model approach to obtain a fast and accurate estimation of the aortic displacement due to the guidewire introduction, exploring various input parameters. The fusion of ROM and morphing tools has not been considered before for EVAR planning and navigation.

2. Materials and methods

2.1. Image acquisition and segmentation

The abdominal aorta of a 75-year-old male patient eligible for EVAR was segmented from a pre-operative CT scan with contrast (pixel spacing: 0.5 mm x 0.5 mm; slice thickness: 1 mm), acquired at St. Olav's hospital, Trondheim (Norway) in accordance with the study protocol approved by the regional ethics committee. Written informed consent was provided by the patient. A segmentation algorithm, based on intensity threshold and morphological operations (e.g. binary opening to keep only the largest connected components), was developed in Python 3.9 to semi-automatically segment the lumen of the abdominal aorta [29]. The iliac arteries were cut at their outlets by a transverse plane defined according to the anatomical reference system shown in Fig. 1 where xy is the frontal plane, xz is the sagittal plane and yz is the transverse plane.

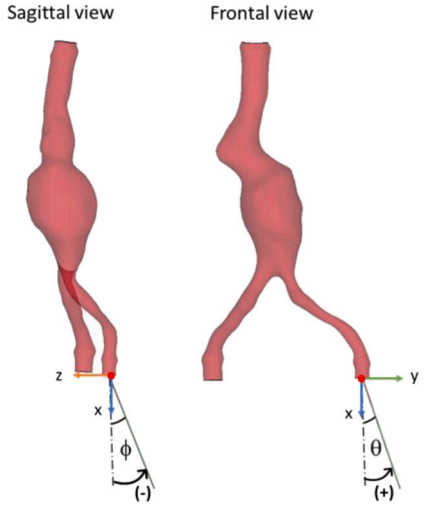

Fig. 1. Description of the insertion angles ϕ and θ in the sagittal and frontal views, respectively. The guidewire rotates around the y and z axes of the depicted reference system in the sagittal and frontal views, respectively.

2.2. Parametric FEA

The simulations were performed with the commercial FE software LS-DYNA (Ansys, Canonsburg, Pennsylvania, USA). The segmented geometry of the aorta was discretized with triangular shell elements, choosing a thickness of 2.5 mm and a characteristic length of 1.4 mm (obtained based on a mesh sensitivity analysis), and modeled as a linear elastic material. The thickness was chosen considering the range reported in literature for abdominal aneurysms [30], the requirements for manufacturing that allowed for in vitro validation [29] and the patient's age [31]. A geometric model of the guidewire was created and discretized with beam elements, selecting a 4 mm length and assuming linear elasticity. The guidewire had a flexible tip, which was modeled with a gradually decreasing elastic modulus. More precisely, it was divided into three parts and the following values of stiffness were applied, respectively: 1, 10 and 50 GPa [10]. A rigid introducer was included to avoid undesired movements of the guidewire outside the vessel.

The insertion of the stiff guidewire in the left iliac artery was simulated by imposing a velocity curve to the most distal node of the guidewire as proposed by Gindre et al. [10]. Previous works [10,29] have shown that the results of the simulations are not sensitive to the insertion speed, within a certain range. Thus, to accelerate ROM development, insertion was performed at an insertion speed of 500 mm/s, with a duration of insertion equal to 1.2 s. The nodes of the proximal and distal extremities of the aortic model were fixed. An Automatic Beams to Surface contact algorithm, based on soft constraint penalty formulation, was applied between the guidewire and the vessel.

The adopted numerical high-fidelity model, described in detail in Emendi et al. [29], was validated against in-vitro experiments that replicate the EVAR procedure.

The above-described FE model was geometrically and physically parameterized through in-house written Python scripts. The investigated parameters and their corresponding range are reported in Table 1.

The range of aortic elasticity, E_{aorta}, was [0.8 – 3] MPa and it was determined based on literature values [32], considering a population

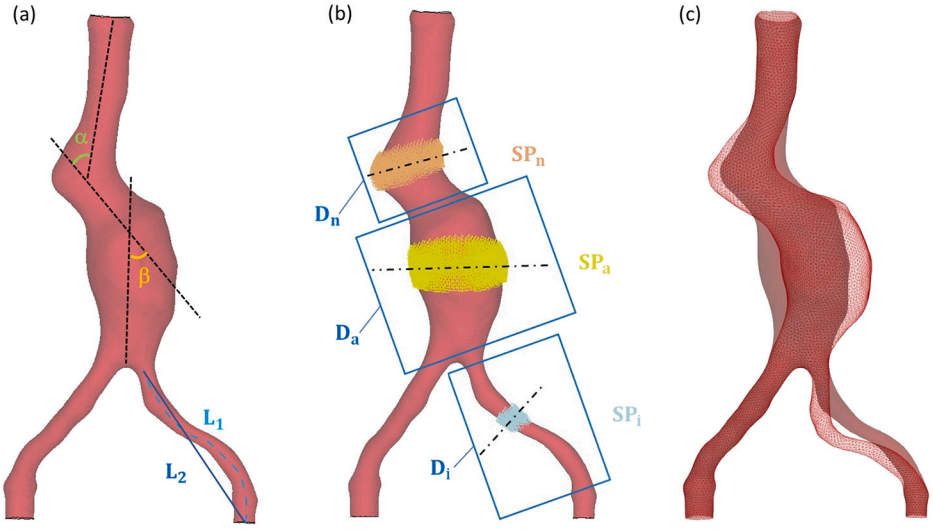

Fig. 2. Description of the morphing actions: (**a**) Morphing parameters: α, supra-renal neck angle; β infra-renal neck angle; L_1 and L_2 that are respectively the length of the left iliac artery and the Euclidean distance between its ending points, these lengths are used to calculate the tortuosity of the iliac artery $\tau = (L_1 \setminus L_2) - 1$ (**b**) Set of source points SP_n, SP_a and SP_i, with the corresponding domains D_n, D_a and D_i. The black dotted lines indicate the direction of translations imposed on each set of source points. (**c**) Example of morphed geometry (wire-frame), overlaid onto the original geometry shown in transparency.

Table 1
Range of the seven explored parameters employed for the FEM parametric model.

Parameter	Description	Range
E_{aorta}	Young's Modulus of aorta	[0.8 – 3] MPa
E_{wire}	Young's Modulus of guidewire	[60 – 200] GPa
ϕ	insertion angle - sagittal plane	[-25 – 0]°
θ	insertion angle - frontal plane	[0 – 20]°
α	supra-renal neck angle	[30 – 55]°
β	infra-renal neck angle	[25 – 60]°
τ	tortuosity of left iliac	[0.09 – 0.15]

of aneurysmatic subjects. For the Young's Modulus of the guidewire, E_{wire}, the minimum and maximum values were set to 60 and 200 GPa, respectively, which correspond to the softest and the stiffest commercial guidewire types available in the market: Amplatz Super Stiff (Boston Scientific) and Lunderquist Extra Stiff (Cook Medical), respectively [11, 33]. The guidewire's insertion angles, ϕ and θ, were defined respectively by rotations around the y and z axis of the anatomical reference frame defined at the outlet of the left iliac artery, as shown in Fig. 1. The spans of ϕ and θ were [-25 – 0]° and [0 – 20]°, respectively. These values respected the given anatomical boundaries and tools' maneuverability, i.e., the presence of the spine, the supine position of the patient and the access from the femoral artery. The supra- and infra-renal neck angles, α and β were defined according to previous works [34,35]. The tortuosity of the iliac artery was defined as follows [36]:

$$\tau = \frac{L_1}{L_2} - 1, \tag{1}$$

where L_1 and L_2 are respectively the length of the left iliac artery and the Euclidean distance between its ending points. In this study, solely the tortuosity of the left iliac artery was considered because the guidewire was inserted through this vessel. The parameters α, β and τ are depicted in Fig. 2 (a). The morphing approach adopted to obtain the geometrical variation linked to α, β and τ is described in section 2.3.

2.3. Morphing set-up

The Python version of the RBF Morph software [37] was used to obtain the morphed configurations of the abdominal aorta in an automated way. Three different sets of source points SP_n, SP_a and SP_i, shown in Fig. 2 (b), were generated using LS-PrePost processor:

1. SP_n, located in the neck region
2. SP_a, placed in the middle part of the aneurysm, e.g. aortic bulge.
3. SP_i, positioned in the middle of the left iliac artery.

On these points, the desired displacement was directly imposed. By applying a translation on the tangential direction of one set of source points at a time, we generated three discrete RBF shape modifiers. The morphing action of each modifier was limited inside the domains, D_n, D_a and D_i defined for the neck region, aneurysm and left iliac, respectively (Fig. 2 (b)). Inside these domains, the nodal displacement was the result of the RBF interpolation algorithm, described in detail in the supplementary material and in [38]. The nodes outside these domains were not affected by the morphing actions. As illustrated, the morphing zones of the three shape modifiers did not overlap. An example of the output of the morphing action is depicted in Fig. 2 (c).

Regarding the range of the aortic shape modifiers, reported in Table 1, we chose values to capture reasonable morphological variations that have clinical meaning: the imposed displacement of SP_n, SP_a and SP_i gave the desired variation of the parameters of interest, α, β and τ (Table 1). The selection of parameters was driven from literature data: severe supra- and infra-renal neck angulation (α and β greater than 60°) are associated with increasing risk of post-operative complications, as type 1A endoleaks [34,39]. High values of iliac tortuosity, τ, are correlated with increasing levels of deformations and more challenging procedures [7]. The combination of the selected morphing parameters enabled us to explore a broad spectrum of possible aortic configurations.

2.4. Reduced order model background

A Reduced Order Model (ROM) is a simplified mathematical representation of a complex system or process that captures its essential behavior while significantly reducing the computational cost and complexity associated with modeling and simulation [40]. There are mainly two distinct approaches in ROM generation: the model-based and the data-driven [41]. The first builds a mathematical model of the system, whereas the second generates a model based on observed data or simulation data, e.g., of a finite element model. In this study, the latter method is adopted and described.

The ROM creation workflow is presented in Fig. 3. Initially, the finite element computational model is considered, named the baseline simulation. A set of parameters is then selected for the modification of the

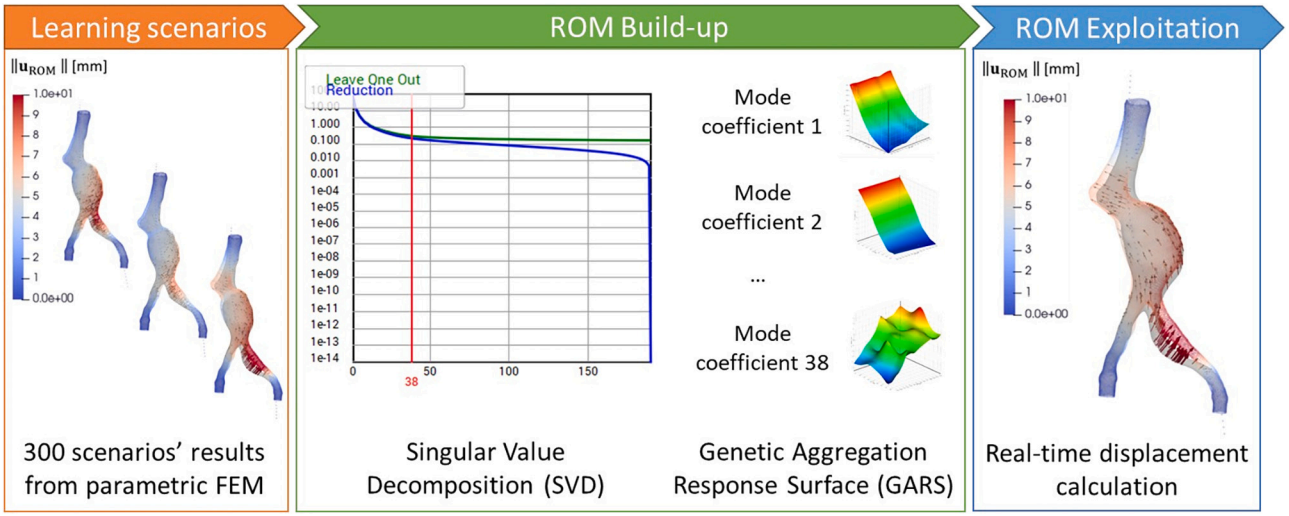

Fig. 3. Description of the main steps of the ROM's workflow: generation of learning scenarios, ROM Build-up and ROM exploitation.

physical and geometrical features of the problem. Afterward, a list of several possible parameter combinations, called scenarios, is built using a Design of Experiments (DOE) method [42,43]. Once the DOE is set, the corresponding simulation results and parametric data are generated in the form of snapshots. Each snapshot consists of a set of data that represents the simulation result of the corresponding scenario.

During the process of building a ROM, the snapshots are compressed into a smaller set of modes using Singular Value Decomposition (SVD). The SVD theorem decomposes a matrix $\mathbf{A}$ into three components:

$$\mathbf{A} = \mathbf{U}\mathbf{S}\mathbf{V}^{\mathrm{T}}, \tag{2}$$

where $\mathbf{U}$ represents the left singular vectors, $\mathbf{S}$ the singular values, and $\mathbf{V}^{\mathrm{T}}$ the right singular vectors [44]. $\mathbf{U}$, $\mathbf{S}$ and $\mathbf{V}^{\mathrm{T}}$ represent the spatial components, the significance of each mode and the temporal components, respectively [45]. The singular values in the diagonal matrix $\mathbf{S}$ are arranged in descending order. By exploiting this mathematical property, the matrix $\mathbf{A}$, which in our case contains all the training data, can be approximated by a linear combination of the first r left singular vectors i.e. $\mathbf{U}_i^*$ with $i = 0$, r, referred to as modes. The accuracy of the approximated matrix $\mathbf{A}_r^*$ depends on the number of r left singular vectors, i.e., increasing the number of r lowers the error tolerance. The approximated matrix $\mathbf{A}_r^*$ in the basis or r modes is given by the following equation:

$$\mathbf{A}_\mathbf{r}^* = \mathbf{U}_\mathbf{r}^* \, \mathbf{S}_\mathbf{r}^* \, \mathbf{V}_r^{\mathrm{T}^*}. \tag{3}$$

The ROM solution of each new input data set can be linearly expressed through a set of scalar coefficients with the Genetic Aggregation Response Surface (GARS) technique [46]. The variable $v(\mathbf{p})$ of a selected point $\mathbf{p}(x, y, z)$ is calculated as the accumulation of the product of the response surface factor and the mode data, mode($\mathbf{p}$), for the total number of selected modes, r:

$$v(\mathbf{p}) = \sum_{i=1}^{r} \mathrm{GARS}_i(\mathbf{p}) \, \mathrm{mode}_i(\mathbf{p}). \tag{4}$$

The GARS finds the best possible response surface based on the selected design of experiments by combining metamodels, settings, kernel variation and polynomial regression.

The ROM is considered successful when it estimates the variable of interest from input combinations that are not included in the training set with sufficient precision.

2.5. ROM set-up

For the generation of the DOE table, the Optimal Space Filling Algorithm was employed. We used a Latin Hypercube Sampling optimized algorithm to better fill the parameters' space. Considering the number of parameters of the studied problem, a total of 300 scenarios was selected and subsequently built using the mechanical and geometrical features described in section 2.2. The corresponding high-fidelity simulations were launched in batch mode employing Bash shell-scripting. The entire computational part was performed using 240 cores (Intel Xeon Gold 6152 CPU @ 2.10 GHz) in task parallelism mode. We opted for task parallelism because individual simulations were independent. After conducting a scalability analysis of the high-fidelity FE simulation, we found out that using 4 cores leads to the minimum computational time which was around 25 minutes. Thus, with 240 cores the 300 snapshots were processed in 5 waves of 60 concurrent simulations. The computational part was completed within 125 minutes (2 hrs 5 minutes) of wall clock time consuming a total of 125 CPU hours.

The extraction of the nodal displacement from the simulation output files and its conversion to a binary file, i.e., snapshot, was conducted using in-house Python scripts. Afterward, the snapshots were imported into ANSYS Twin Builder (ANSYS® Electronics Desktop TM - Release 22R2). 200 scenarios were used for the ROM training while the remaining 100 were employed for the ROM validation. The selection of the size of the training and the validation set was made based on a sensitivity analysis of the reduction root mean square (RMS) error, which is defined as

$$e_{\mathrm{red}}^{\mathrm{RMS}} = \frac{\|\mathbf{A} - \mathbf{A}_\mathbf{r}^*\|}{\|\mathbf{A}\|}, \tag{5}$$

and signifies the loss of information that occurs when switching from the full learning data set $\mathbf{A}$ to the r representative modes $\mathbf{A}_\mathbf{r}^*$ as described in Section 2.4.

Table 2
Sensitivity analysis of reduction root mean square (RMS) error with respect to the size of the training dataset.

Size of training dataset	Reduction RMS error %
50	0.504
100	0.342
150	0.252
200	0.200
250	0.190

As illustrated in Table 2, by increasing the size of the training data, the reduction RMS error becomes lower. Taking into consideration the available data resources and aiming for a reduction RMS error below 0.2%, we opted for a ratio of training and validation data size equal to 2:1.

After deciding on the size of the two subsets, we chose which snapshots would be included for the ROM training and which for the validation based on the optimal distribution algorithm. This algorithm, embedded in ANSYS Twin Builder, selects the ROM training snapshots with the optimal spatial distribution in terms of input parameters. Proceeding with SVD, we identified the best compromise between the desired accuracy and the number of selected singular values by analyzing two curves: the reduction curve which represents the accuracy of snapshot reconstruction with respect to the learning subset and the Leave One Out curve which represents this accuracy with respect to snapshots outside the learning set. As depicted in Fig. 3, by selecting 38 r modes to capture the problem's physics, we got a reduction RMS error equal to 0.2%. Additionally, the Leave One Out curve becomes flat for more than 38 r modes, which signifies that including the next mode in the decomposition, would have a negligible effect in terms of accuracy.

With regards to the ROM validation, four different types of errors were calculated for each validation scenario: the relative reduction and ROM errors, $e^{\text{rel}}_{\text{red}}$ and $e^{\text{rel}}_{\text{ROM}}$, respectively, which are normalized with the absolute value of the full order solution, i.e. $\mathbf{u}_{\text{ref}}$, and the absolute reduction and ROM errors, $e^{\text{abs}}_{\text{red}}$ and $e^{\text{abs}}_{\text{ROM}}$, respectively. These errors were defined as follows:

$$e^{\text{rel}}_{\text{red}} = \frac{\|\mathbf{u}_{\text{ref}} - \mathbf{u}_{\text{proj}}\|}{\|\mathbf{u}_{\text{ref}}\|}, \tag{6}$$

$$e^{\text{rel}}_{\text{ROM}} = \frac{\|\mathbf{u}_{\text{ref}} - \mathbf{u}_{\text{ROM}}\|}{\|\mathbf{u}_{\text{ref}}\|}, \tag{7}$$

$$e^{\text{abs}}_{\text{red}} = max(\mathbf{u}_{\text{ref}} - \mathbf{u}_{\text{proj}}), \tag{8}$$

$$e^{\text{abs}}_{\text{ROM}} = max(\mathbf{u}_{\text{ref}} - \mathbf{u}_{\text{ROM}}), \tag{9}$$

where $\mathbf{u}_{\text{ref}}$ indicates the high-fidelity FEM nodal displacement vector, $\mathbf{u}_{\text{proj}}$ is the projection of the $\mathbf{u}_{\text{ref}}$ in the r modes basis (i.e. solution after SVD reduction), and $\mathbf{u}_{\text{ROM}}$ stands for the ROM predicted displacement vector for all the nodes. The interpolation error triggered by the GARS can be obtained as the subtraction of the reduction error from the ROM error. Further information with regards to the ROM build-up, validation and application can be found on ANSYS user-guide [47].

3. Results

3.1. ROM validation

A statistical analysis of the relative reduction and ROM error is described for the assessment of the model's trustworthiness. The distribution of the relative reduction error, $e^{\text{rel}}_{\text{red}}$ (%), i.e., the error deriving from the approximation of the deformation field due to keeping the first 38 r modes of the SVD, is presented in Fig. 4 (a) for the displacement field of all the validation scenarios. In Fig. 4 (b) the relative ROM error, $e^{\text{rel}}_{\text{ROM}}$ (%) is displayed and it represents the sum of the relative reduction error and GARS interpolation error.

The average relative reduction error, $e^{\text{rel}}_{\text{red}}$ (%), is equal to 0.26 ± 0.06%. In 74% of the validation scenarios $e^{\text{rel}}_{\text{red}}$ (%) varies between 0.20% and 0.30%. A $e^{\text{rel}}_{\text{red}}$ (%) of more than 0.4% occurs for only three instances (Fig. 4 (a)).

With regards to the relative ROM error, more than 75% of the validation scenarios have a $e^{\text{rel}}_{\text{ROM}}$ below 4.0% (Fig. 4(b)). The average $e^{\text{rel}}_{\text{ROM}}$ is equal to 3.28 ± 1.00%.

In Fig. 5, the absolute deformation error, $e^{\text{abs}}_{\text{ROM}}$, of five chosen validation scenarios, among the least accurate ones, is presented.

For the illustrated cases, the average relative ROM error, $e^{\text{rel}}_{\text{ROM}}$, is equal to 3.28%. The maximum $e^{\text{abs}}_{\text{ROM}}$ is 0.32 mm and is observed in validation scenario (d) close to the origin of the left iliac artery. The largest discrepancy between the ROM prediction and the high-fidelity solution is detected in the same region for all scenarios. The aneurysmatic bulge deformation is predicted with an average error of 0.17 mm on validation scenarios (b), (c) and (e). The prediction error, $e^{\text{abs}}_{\text{ROM}}$, of the aortic neck region is below 0.1 mm for scenarios (c), (d), (e) and 0.20 mm for scenarios (a) and (b).

3.2. ROM exploitation

After the successful ROM training and validation, hands-on deployment of the pipeline was carried out. As exhibited in Fig. 6, we selected a trial parametric set-up ($E_{\text{aorta}} = 1.5$ MPa, $E_{\text{wire}} = 180$ GPa, $\phi = -5°$, $\theta = 7°$, $\alpha = 48°$, $\beta = 52°$, $\tau = 0.15$) and the calculated aortic displacement was depicted within few seconds.

The left iliac artery experiences the greatest deformations, reaching up to 1.3 mm, straightening towards the posterior and left patient-oriented direction. The aneurysmatic bulge, the aortic neck and the right iliac artery are displaced towards the right superior direction. The magnitude of this displacement is 6.5 mm on average. The neck region is moving anteriorly in contrast with the aneurysm and the iliac arteries. The sagittal side of the aneurysmatic sac undergoes high displacements, almost 9.5 mm, to the superior and right direction.

3.3. Qualitative analysis of the influence of the DOE parameters

The following remarks resulted from the examination of the individual impact of each parameter on the 3D aortic displacement.

In Fig. 7, eight example cases, investigating the impact of aortic elasticity and guidewire's stiffness on the aortic deformation field, are shown.

For descending values of E_{aorta}, the left iliac artery and the left side region of the aneurysm are encountering increasing displacements, with a maximum value of 1.2 mm in the case of $E_{\text{aorta}} = 0.9$ MPa. The aortic neck region is almost unaffected by the explored values of aortic elasticity. Adopting $E_{\text{aorta}} = 2.9$ MPa, instead of 0.9 MPa, leads to a more uniform deformation map with maximum displacements reduced by 60%. A similar displacement field, i.e., almost equal deformation vectors throughout the whole aorta, is obtained for increasing E_{aorta} and decreasing E_{wire}.

The effect of choosing different insertion angles, ϕ and θ, is presented in Fig. 8. As the magnitude of ϕ drops, the displacement of the left iliac artery and part of the left side of the aneurysm increases. The remaining geometry stays almost unaltered. For the investigated scenarios, the peak deformations take place for ϕ equals to -5° and extend up to 8.5 mm.

The magnitude of θ has negligible effect on the aortic displacement field. For the investigated angles, the most deformed nodes are concentrated on the left iliac artery and the left side of the aneurysmatic sac.

The effect of the left iliac tortuosity is illustrated in Fig. 9. Low tortuosity values result mainly in displacement of left iliac artery's origin and left aneurysmatic side in the postero-superior direction and leftward. Moving to higher tortuosity values, above 0.12, different aortic motions take place: the effect of the straightening on the left iliac artery increases, with higher displacement vectors and greater displacement components in the superior direction; the neck region and the aneurysm are displaced towards the right superior direction.

4. Discussion

In this work, a ROM was developed for the fast and accurate estimation of the aortic deformation due to the insertion of a guidewire (during EVAR) as a function of seven mechanical, morphological and clinical parameters. Starting from the abdominal aortic geometry of a patient eligible for EVAR, we introduced the morphological modifiers α, β, and τ using RBF mesh morphing technique. By tuning these parameters, we were able to produce a wide range of possible similar patient configurations. The elasticity of the aortic wall (E_{aorta}) and the guidewire (E_{wire}) as well as the wire's insertion angles (ϕ, θ) were explored. 300 combinations of these seven adopted parameters were examined as potential

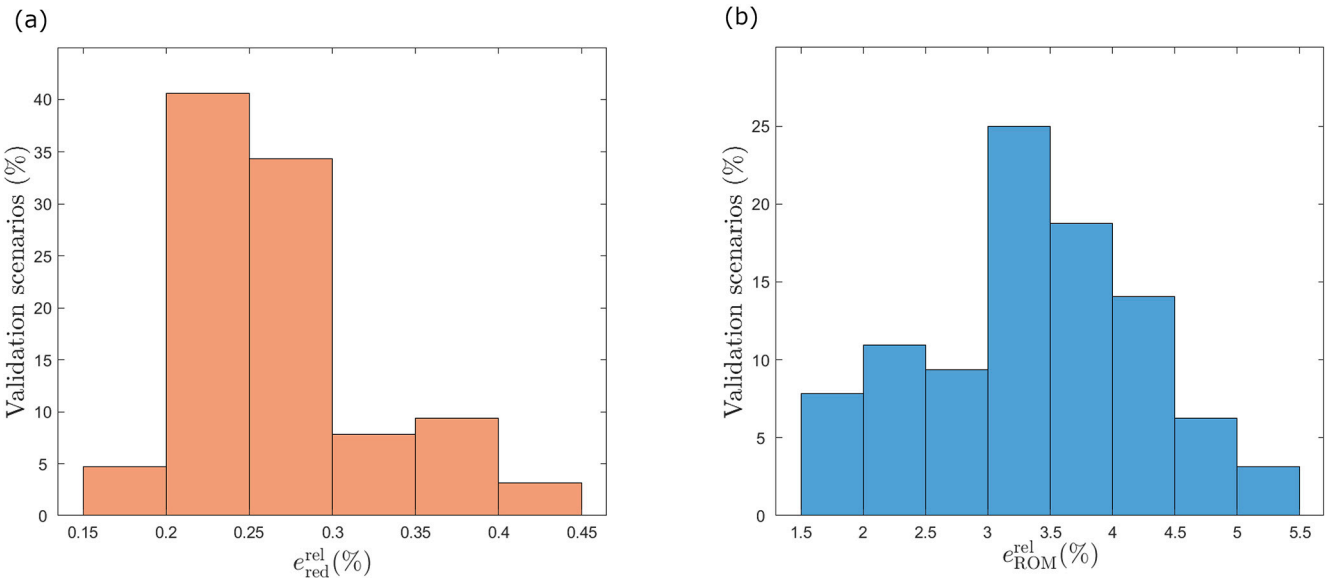

Fig. 4. Distribution of the relative reduction error $e^{\text{rel}}_{\text{red}}$ (%), (a) and the relative ROM error $e^{\text{rel}}_{\text{ROM}}$ (%), (b) on the validation scenarios.

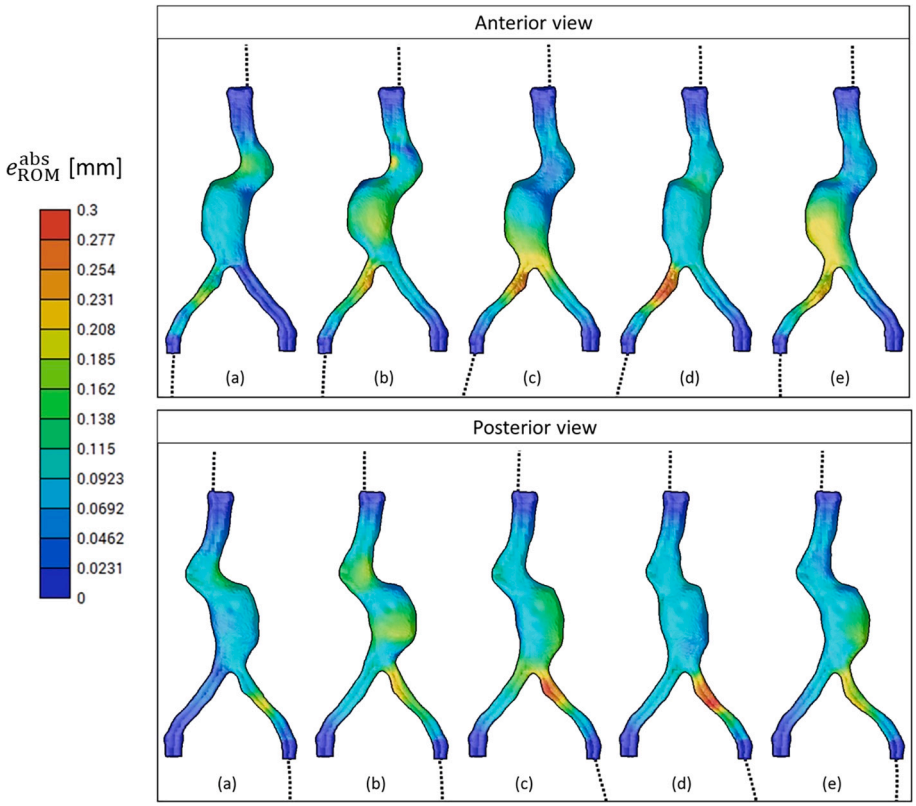

Fig. 5. Color map of the ROM absolute error, $e^{\text{abs}}_{\text{ROM}}$ for five validation scenarios (a), (b), (c), (d) and (e), anterior and posterior views. The values are displayed on the final deformed geometries resulting from the guidewire interaction.

EVAR navigation cases, i.e., scenarios, which were thereafter used for the ROM building. The accuracy of the generated model was statistically assessed. The ROM was validated against 100 random scenarios and its mean normalized prediction error, $e^{\text{rel}}_{\text{ROM}}$ (eq. (7)), was found below 5.5% across all examined scenarios (Fig. 4b). Lastly, the ROM exploitation was performed, demonstrating the almost real-time calculation of the 3D aortic wall displacement during EVAR.

As a supplement to this study, we conducted a preliminary qualitative analysis of the effect of the adopted parameters on the aortic displacement field. According to our findings, low E_{aorta} and high E_{wire} values tend to cause large deformations ($\sim$ 1.3 mm) near the root of the left iliac artery. The aortic stiffness is linked to ageing, atherosclerosis and presence of calcifications, common in patients with abdominal aortic aneurysms, and it has been shown to affect the aortic interaction with the guidewire [7,12]. With regards to the stiff guidewire, clinicians have different types of wires available, with a minimum Young's modulus of 60 GPa (Amplatz Super Stiff) and a maximum of 200 GPa (Lunderquist Extra Stiff) [33]. Therefore, the ROM prediction could be

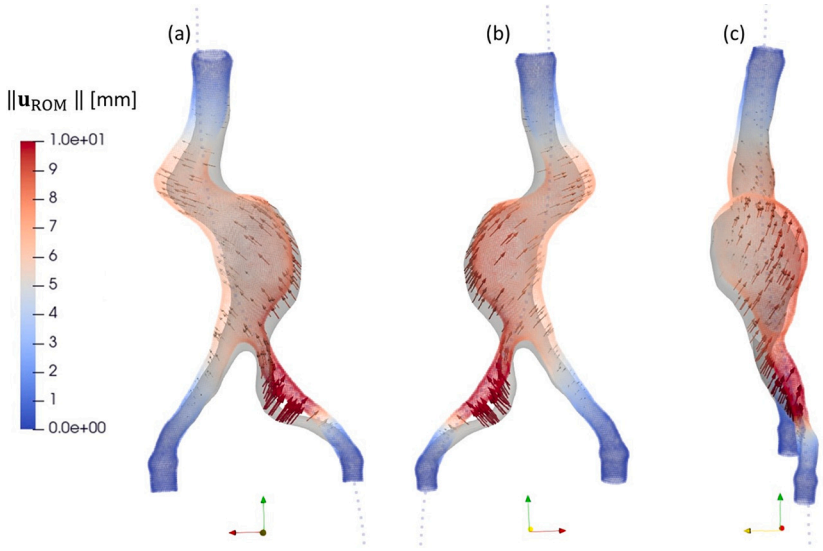

Fig. 6. Example of ROM output for the following chosen parameters: $E_{aorta} = 1.5$ MPa, $E_{wire} = 180$ GPa, $\phi = -5°$, $\theta = 7°$, $\alpha = 48°$, $\beta = 52°$, $\tau = 0.15$. The nodal displacement vectors, $\mathbf{u}_{ROM}$, defined from the initial (light grey) to the final (color-mapped by displacement magnitude) aortic configuration, are presented. (a) Anterior view, (b) Posterior view, (c) Sagittal view.

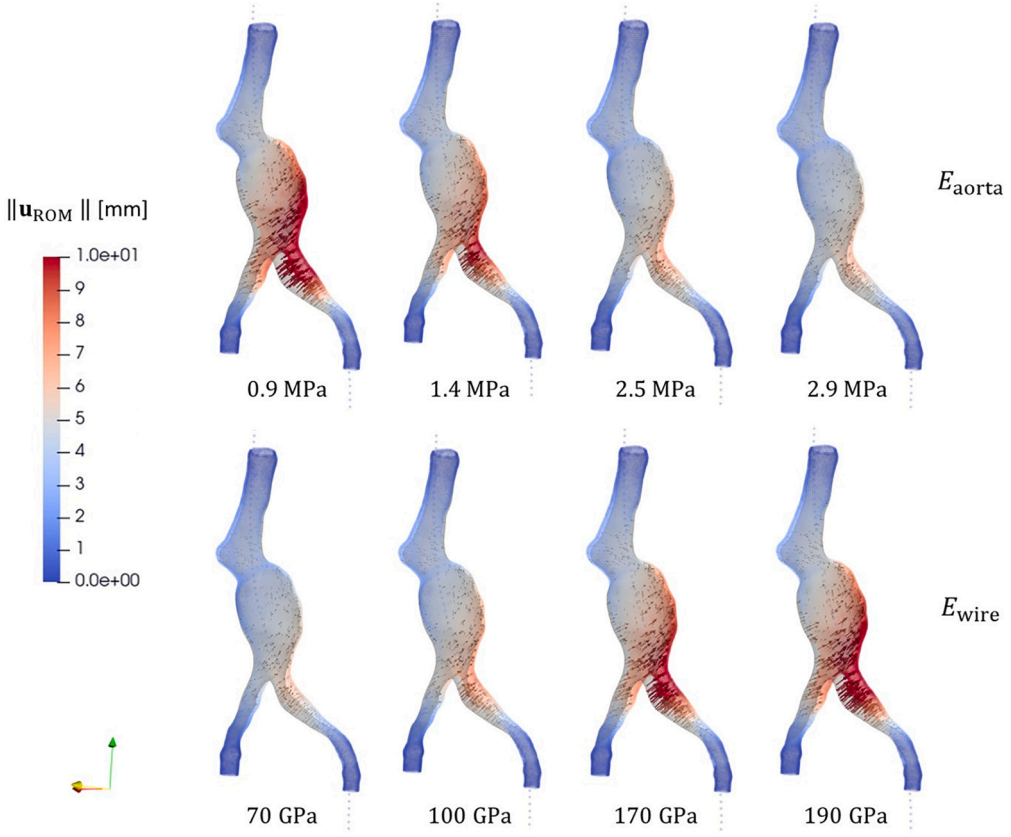

Fig. 7. Aortic displacement as a function of E_{aorta} and E_{wire} parameters. The initial aortic configuration is shown in light grey. The arrows indicate the guidewire-induced displacement vectors, $\mathbf{u}_{ROM}$. The deformed aortic configuration is colored by the displacement vector magnitude, $\|\mathbf{u}_{ROM}\|$. The remaining parameters were fixed as follows: $\phi = 0°$, $\theta = 0°$, $\alpha = 44.2°$, $\beta = 32.8°$, $\tau = 0.12$.

helpful for choosing the appropriate tool, as a compromise between navigability and potential tissue damage. Our study also showed that high τ values trigger an increased displacement of the left iliac artery towards the posterior direction, while the rest of the geometry moves towards the anterior right direction; all the aortic nodes are displaced superiorly. This is in agreement with what has been already highlighted in literature: the straightening effect of the guidewire on the common iliac artery increases in case of severe iliac tortuosity values [7].

Examining the effect of the insertion angles, we found that for low values of ϕ, the deformations are higher close to the left iliac artery. On the other hand, the magnitude of θ does not seem to significantly affect the resulting deformations. Exploiting our ROM, clinicians can

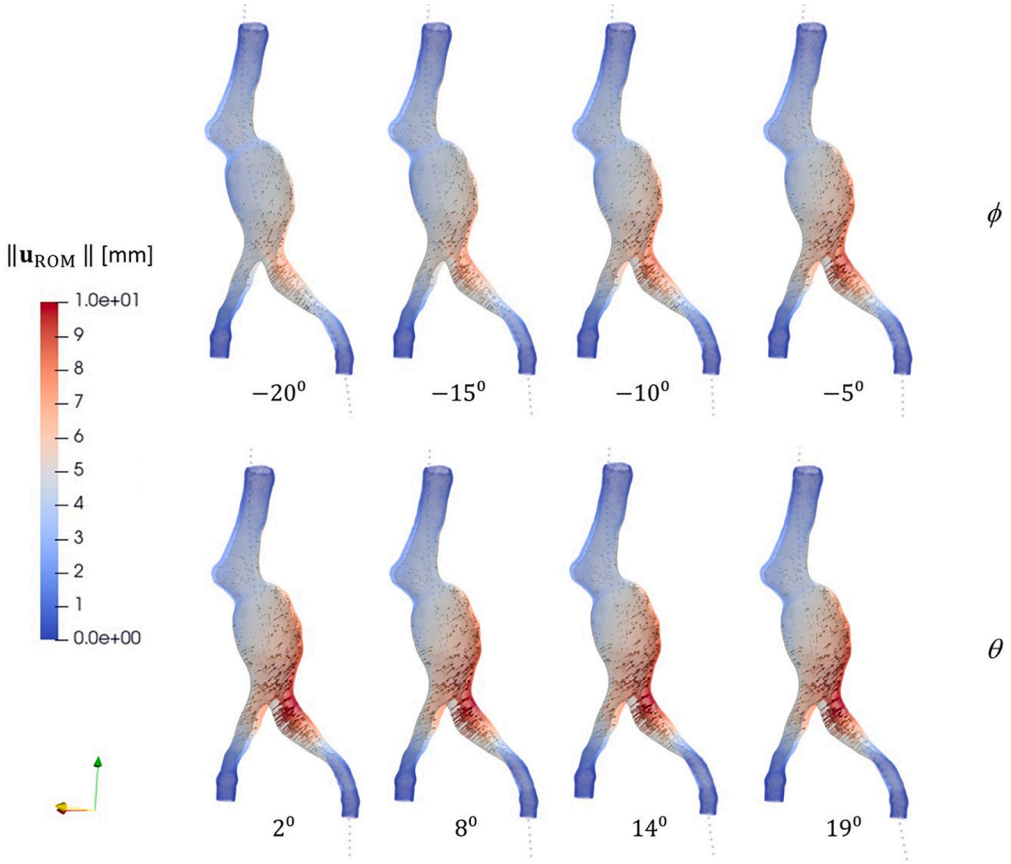

Fig. 8. Aortic displacement obtained from ROM as a function of insertion angles, ϕ and θ. The initial aortic configuration is shown in light grey. The arrows indicate the guidewire-induced displacement vectors. The deformed aortic configuration is colored by the displacement vector magnitude, $\|\mathbf{u}_{ROM}\|$. The remaining parameters were set as follows: $E_{aorta} = 1.4$ MPa, $E_{wire} = 150$ GPa, $\alpha = 44.2^\circ$, $\beta = 32.8^\circ$, $\tau = 0.12$.

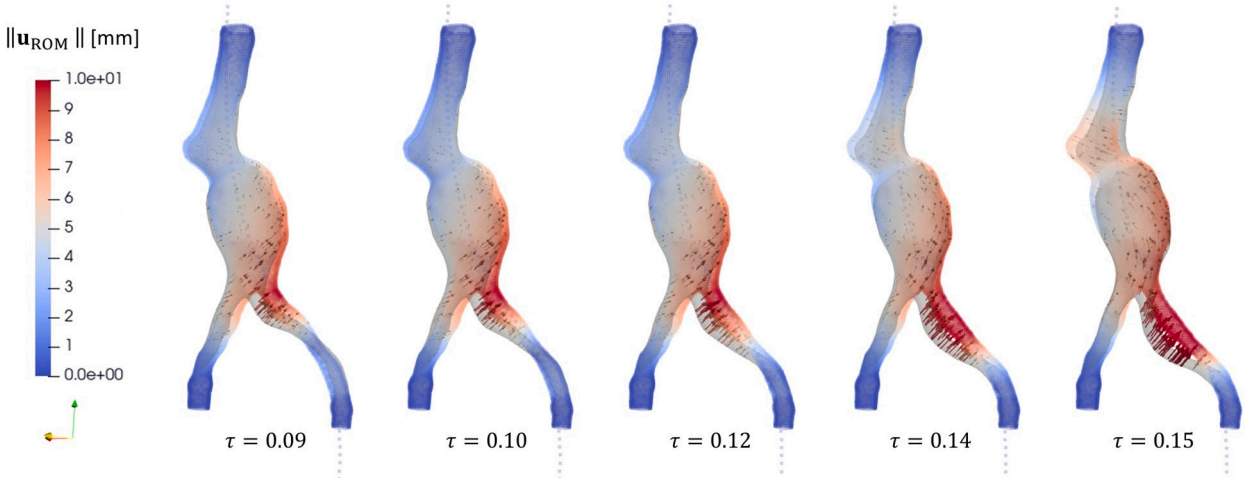

Fig. 9. Aortic displacement obtained from ROM as a function of left iliac tortuosity, τ. The initial aortic configuration is shown in light grey. The arrows indicate the guidewire-induced displacement vectors. The deformed aortic configuration is colored by the displacement vector magnitude, $\|\mathbf{u}_{ROM}\|$. The remaining parameters were fixed as follows: $E_{aorta} = 1.4$ MPa, $E_{wire} = 150$ GPa, $\phi = 0^\circ$, $\theta = 0^\circ$, $\alpha = 44.2^\circ$, $\beta = 32.8^\circ$.

select the appropriate orientation of guidewire insertion, that minimizes deformations and stresses on the aortic wall. For instance, higher values of the angle ϕ angles lead to reduced aortic displacements in the studied model.

In agreement with previous works, which estimate the guidewire-induced aortic deformations by means of clinical acquisitions [7] and finite element models [48], we observed that the area with the highest values of displacement is located at the root of the common iliac artery on the side of insertion for all the considered ROM scenarios. In detail, the study by Kaladji et al. [48] reports a magnitude of displacement equal to 10.2 ± 3.3 mm for the cannulated iliac artery, occurring mostly in the posterior-superior direction, similar to what is noticed in the illustrated case (Fig. 6).

Compared to previous works which focused on high-fidelity models of guidewire insertion [10–12], the proposed workflow speeds up the displacement calculation in two ways. The mesh-morphing technique

enables to explore a wide spectrum of aortic configurations without image segmentation. The total morphing time for all the scenarios is around 30 minutes. Employing the ROM approach, the solution's calculation takes a few seconds whereas solving the full order model requires 25 minutes for each scenario. High-fidelity models are not compatible with the tight clinical intra-operative time frame. On the other hand, the ROM herein proposed takes 135 minutes to be built once, i.e. 125 minutes for the snapshots generation and 10 minutes for the ROM build-up, then it is ready to be used and provides real-time response. The ROM data generation time can be further reduced by using larger High-Performance Computing (HPC) facilities. In addition to the above-mentioned timeframes, segmentation and meshing procedures take 30 minutes on average, hence the total ROM pipeline is completed within 3 hours and 15 minutes. Thus, the proposed approach would be within the pre-operative timeframe for non-acute cases and once built, compatible with intra-operative usage.

With regards to the ROM prediction error, it is kept below 0.32 mm for all the validation scenarios (Fig. 5). This error is comparable to the spatial resolution of the currently adopted imaging modality for EVAR navigation, i.e., DSA, which is about 0.5 mm [49,50]. In order to further reduce this error, additional ROM training is required. However, the choice of this training set-up was made as a compromise between the computational cost and the ROM accuracy. In addition, the highest errors are detected only in a few scenarios, i.e., 8% of our validation scenarios and are always localized at a few nodes of the cannulated iliac artery.

This study presents some limitations that can be tackled in future works. The proposed workflow can be applied to more tortuous and challenging anatomies to examine the behavior of the ROM in demanding cases. To extend this study to a population of patients and standardize the considered parameters, including the guidewire's insertion angle, it is desirable to cut the iliac arteries at a known distance from the aortic bifurcation using a plane normal to the centerline of each iliac artery; thus, the insertion angles can be determined starting from the normal of the plane itself. The wall thickness of the aorta is variable, however, in this study was assumed uniform, as in previous works [10,11]. More realistic boundary conditions could be considered, including the effect of the anatomical structures surrounding the abdominal aorta, that can be modeled for example as elastic springs, as proposed by Gindre et al. [10], or as a discretized volume of perivascular tissue [11]. However, the uncertainties related to the choice of the springs' stiffness or mechanical properties of the perivascular tissue should be further investigated. The effect of adopting an hyperelastic material model [51] along with the application of pre-stress [52,53], caused by arterial pressure, should be investigated in the future to get one step closer to reality. Lastly, the high-fidelity model should be validated against in vivo intra-operative acquisitions before the ROM approach can be translated into clinical practice.

5. Conclusions

A fast and precise prediction of the aortic displacement field, caused by the guidewire's insertion during EVAR, was carried out by building an interactive and user-friendly ROM environment. This approach allows a comprehensive analysis of the presented clinical problem spanning various parameters while avoiding re-computing the simulations. Thus, it shows the potential to support the clinicians' decision-making process pre- and intra-operatively, reducing the use of radiation and contrast. The reduced order model could be used for patient specific rehearsal, in combination with EVAR simulators, which currently lack the biomechanical aspect of the interaction between the tools and the phantoms [54]. Applying this strategy intra-operatively poses an intriguing upcoming challenge that could potentially impact clinical practice.

Ethical approval

This study was reviewed and approved by the NTNU/REK midt, Faculty of medicine, PO Box 8905, 7491 Trondheim, Norway—Application ID 2016/533. The patients provided their written informed consent to participate in this study.

Funding

The research has received funding from the European Union's Horizon 2020 research and innovation programme under the Marie Skłodowska-Curie grant agreement No. 859836, MeDiTATe: "The Medical Digital Twin for Aneurysm Prevention and Treatment".

CRediT authorship contribution statement

Monica Emendi: Conceptualization, Methodology, Software, Writing – original draft, Writing – review & editing, Formal analysis, Data curation. **Eirini Kardampiki:** Conceptualization, Methodology, Software, Writing – original draft, Writing – review & editing, Formal analysis, Data curation. **Karen-Helene Støverud:** Conceptualization, General guidance, Writing – review & editing. **Antonio Martinez Pascual:** Support with ROM implementation, Writing – review & editing. **Leonardo Geronzi:** Support with the RBF mesh morphing application, Writing – review & editing. **Sigrid Kaarstad Dahl:** General guidance, Writing – review & editing. **Victorien Prot:** Methodology, General guidance, Writing – review & editing. **Paal Skjetne:** General guidance, Writing – review & editing. **Marco Evangelos Biancolini:** Methodology, Funding, Writing – review & editing.

Declaration of competing interest

The authors declare no conflicts of interest.

Appendix A. Supplementary material

Supplementary material related to this article can be found online at https://doi.org/10.1016/j.medengphy.2024.104229.

References

[1] Kim HO, Yim NY, Kim JK, Kang YJ, Lee BC. Endovascular aneurysm repair for abdominal aortic aneurysm: a comprehensive review. Korean J Radiol 2019;20:1247–65.
[2] Daye D, Walker TG. Complications of endovascular aneurysm repair of the thoracic and abdominal aorta: evaluation and management. Cardiovasc Diagn Ther 2018;8:S138.
[3] Pagnozzi AM, Dowson N, Cowled P, Thurston B, Fitridge R. Iliac artery tortuosity, calcification and abnormal shape augment aortic aneurysm anatomy in predicting complications after endovascular aneurysm repair. SN Compr Clin Med 2022;4:203.
[4] Gokani V, Fishwick N, Choke E, Bown M, Sayers R. 'Trial of stiff guidewire': a useful adjunct to determining suitability for endovascular aneurysm repair. EJVES Extra 2012;24:e23–4.
[5] Cuypers P, Laheij R, Buth J. Which factors increase the risk of conversion to open surgery following endovascular abdominal aortic aneurysm repair? Eur J Vasc Endovasc Surg 2000;20:183–9. https://doi.org/10.1053/ejvs.2000.1167. https://www.sciencedirect.com/science/article/pii/S1078588400911675.
[6] Koutouzi G, Pfister M, Breininger K, Hellström M, Roos H, Falkenberg M. Iliac artery deformation during EVAR. Vascular 2019;27:511–7.
[7] Cercenelli L, Bortolani B, Tiberi G, Mascoli C, Corazza I, Gargiulo M, et al. Characterization of vessel deformations during evar: a preliminary retrospective analysis to improve fidelity of endovascular simulators. J Surg Educ 2018;75:1096–105.
[8] Dupont C, Kaladji A, Rochette M, Saudreau B, Lucas A, Haigron P. Numerical simulation of fenestrated graft deployment: anticipation of stent graft and vascular structure adequacy. Int J Numer Methods Biomed Eng 2021;37:e03409.
[9] Derycke L, Avril S, Millon A. Patient-specific numerical simulations of endovascular procedures in complex aortic pathologies: review and clinical perspectives. J Clin Med 2023;12:766.
[10] Gindre J, Bel-Brunon A, Kaladji A, Duménil A, Rochette M, Lucas A, et al. Finite element simulation of the insertion of guidewires during an evar procedure: example of a complex patient case, a first step toward patient-specific parameterized models. Int J Numer Methods Biomed Eng 2015;31:e02716.

[11] Mohammadi H, Lessard S, Therasse E, Mongrain R, Soulez G. A numerical preoperative planning model to predict arterial deformations in endovascular aortic aneurysm repair. Ann Biomed Eng 2018;46:2148–61.
[12] McLennan S, Soulez G, Mongrain R, Mohammadi H, Pfister M, Lessard S, et al. Impact of calcification modelling to improve image fusion accuracy for endovascular aortic aneurysm repair. Int J Numer Methods Biomed Eng 2021;38. https://doi.org/10.1002/cnm.3556.
[13] Daoudal A, Gindre J, Lalys F, Kafi M, Dupont C, Lucas A, et al. Use of numerical simulation to predict iliac complications during placement of an aortic stent graft. Ann Vasc Surg 2019;61:291–8.
[14] Maurel B, Hertault A, Sobocinski J, Le Roux M, Gonzalez TM, Azzaoui R, et al. Techniques to reduce radiation and contrast volume during evar. J Cardiovasc Surg 2014;55:123–31.
[15] Condino S, Calabrò E, Alberti A, Parrini S, Cioni R, Berchiolli RN, et al. Simultaneous tracking of catheters and guidewires: comparison to standard fluoroscopic guidance for arterial cannulation. Eur J Vasc Endovasc Surg 2014;47:53–60.
[16] Jäckle S, Garcia-Vázquez V, von Haxthausen F, Eixmann T, Sieren M, Schulz-Hildebrandt H, et al. 3d catheter guidance including shape sensing for endovascular navigation; 2020. p. 3. https://doi.org/10.1117/12.2548094.
[17] Jones DW, Stangenberg L, Swerdlow NJ, Alef M, Lo R, Shuja F, et al. Image fusion and 3-dimensional roadmapping in endovascular surgery. Ann Vasc Surg 2018;52:302–11.
[18] Vega JM, Le Clainche S. Higher order dynamic mode decomposition and its applications. Academic Press; 2020.
[19] Dal Santo N, Manzoni A, Pagani S, Quarteroni A, et al. Reduced-order modeling for applications to the cardiovascular system. In: Applications. Berlin, Germany: De Gruyter; 2020. p. 251–78.
[20] Fossan FE, Müller LO, Sturdy J, Bråten AT, Jørgensen A, Wiseth R, et al. Machine learning augmented reduced-order models for ffr-prediction. Comput Methods Appl Mech Eng 2021;384:113892. https://doi.org/10.1016/j.cma.2021.113892. https://www.sciencedirect.com/science/article/pii/S0045782521002292.
[21] Kardampiki E, Vignali E, Haxhiademi D, Federici D, Ferrante E, Porziani S, et al. The hemodynamic effect of modified Blalock–Taussig shunt morphologies: a computational analysis based on reduced order modeling. Electronics 2022;11:1930.
[22] Ballarin F, Faggiano E, Ippolito S, Manzoni A, Quarteroni A, Rozza G, et al. Fast simulations of patient-specific haemodynamics of coronary artery bypass grafts based on a POD–Galerkin method and a vascular shape parametrization. J Comput Phys 2016;315:609–28. https://doi.org/10.1016/j.jcp.2016.03.065. https://www.sciencedirect.com/science/article/pii/S0021999116300304.
[23] Bertagna L, Veneziani A. A model reduction approach for the variational estimation of vascular compliance by solving an inverse fluid–structure interaction problem. Inverse Probl 2014;30:055006.
[24] Bisighini B, Aguirre M, Biancolini ME, Trovalusci F, Perrin D, Avril S, et al. Machine learning and reduced order modelling for the simulation of braided stent deployment. Front Physiol 2023;14:508.
[25] Mynard JP, Alastruey J. Special issue on reduced order modelling for cardiovascular problems; 2022.
[26] Groth C, Porziani S, Biancolini M, Costa E, Celi S, Capellini K, et al. The medical digital twin assisted by reduced order models and mesh morphing. In: International CAE conference, vol. 10. 2018.
[27] Geronzi L, Martinez A, Rochette M, Yan K, Bel-Brunon A, Haigron P, et al. Computer-aided shape features extraction and regression models for predicting the ascending aortic aneurysm growth rate. Comput Biol Med 2023:107052.
[28] Biancolini ME, Capellini K, Costa E, Groth C, Celi S. Fast interactive cfd evaluation of hemodynamics assisted by rbf mesh morphing and reduced order models: the case of ataa modelling. Int J Interact Des Manuf 2020;14:1227–38.
[29] Emendi M, Støverud K-H, Tangen GA, Ulsaker H, Manstad-Hulaas F, Di Giovanni P, et al. Prediction of guidewire-induced aortic deformations during evar: a finite element and in-vitro study. Front Physiol 2023;14.
[30] Raghavan ML, Kratzberg J, de Tolosa EMC, Hanaoka MM, Walker P, da Silva ES. Regional distribution of wall thickness and failure properties of human abdominal aortic aneurysm. J Biomech 2006;39:3010–6.
[31] Rosero EB, Peshock RM, Khera A, Clagett P, Lo H, Timaran CH. Sex, race, and age distributions of mean aortic wall thickness in a multiethnic population-based sample. J Vasc Surg 2011;53:950–7.
[32] Vallabhaneni SR, Gilling-Smith GL, How TV, Carter SD, Brennan JA, Harris PL. Heterogeneity of tensile strength and matrix metalloproteinase activity in the wall of abdominal aortic aneurysms. J Endovasc Ther 2004;11:494–502.
[33] Harrison G, How T, Vallabhaneni SR, Brennan J, Fisher R, Naik J, et al. Guidewire stiffness: what's in a name? J Endovasc Ther 2011;18:797–801. https://doi.org/10.1583/11-3592.1.
[34] Kim T-H, Jang H-J, Choi YJ, Lee CK, Kwon SW, Shim W-H. Kilt technique as an angle modification method for endovascular repair of abdominal aortic aneurysm with severe neck angle. Ann Thorac Cardiovasc Surg 2017;23:96–103.
[35] van Keulen JW, Moll FL, Tolenaar JL, Verhagen HJ, van Herwaarden JA. Validation of a new standardized method to measure proximal aneurysm neck angulation. J Vasc Surg 2010;51:821–8. https://doi.org/10.1016/j.jvs.2009.10.114. https://www.sciencedirect.com/science/article/pii/S0741521409022629.
[36] Piccinelli M, Veneziani A, Steinman DA, Remuzzi A, Antiga L. A framework for geometric analysis of vascular structures: application to cerebral aneurysms. IEEE Trans Med Imaging 2009;28:1141–55.
[37] Rbf morph website, 2023. https://www.rbf-morph.com/.
[38] Biancolini ME, et al. Fast radial basis functions for engineering applications. Springer; 2017.
[39] Mathlouthi A, Locham S, Dakour-Aridi H, Black JH, Malas MB. Impact of suprarenal neck angulation on endovascular aneurysm repair outcomes. J Vasc Surg 2020;71:1900–6. https://doi.org/10.1016/j.jvs.2019.08.250. https://www.sciencedirect.com/science/article/pii/S0741521419323092.
[40] Benner P, Ohlberger M, Patera A, Rozza G, Urban K, et al. Model reduction of parametrized systems; 2017.
[41] Formentin S, van Heusden K, Karimi A. Model-based and data-driven model-reference control: a comparative analysis. In: 2013 European control conference (ECC); 2013. p. 1410–5.
[42] Eriksson L, Johansson E, Kettaneh-Wold N, Wikström C, Wold S. Design of experiments, principles and applications. Stockholm: Learn Ways AB; 2000.
[43] Antony J. Design of experiments for engineers and scientists. Elsevier; 2014.
[44] Wall ME, Rechtsteiner A, Rocha LM. Singular value decomposition and principal component analysis. In: A practical approach to microarray data analysis; 2003. p. 91–109.
[45] Ientilucci EJ. Using the singular value decomposition. Technical report. Rochester, New York, United States: Rochester Institute of Technology; 2003.
[46] Khuri AI, Mukhopadhyay S. Response surface methodology. Wiley Interdiscip Rev: Comput Stat 2010;2:128–49.
[47] ANSYS Inc. Twin builder help. Version 22.2 ed.; 2022.
[48] Kaladji A, Dumenil A, Castro M, Cardon A, Becquemin J-P, Bou-Saïd B, et al. Prediction of deformations during endovascular aortic aneurysm repair using finite element simulation. Comput Med Imaging Graph 2013;37:142–9.
[49] Ota H, Takase K, Rikimaru H, Tsuboi M, Yamada T, Sato A, et al. Quantitative vascular measurements in arterial occlusive disease. Radiographics 2005;25:1141–58.
[50] Guimaraes M, Schönholz C, Uflacker R, Huda W. Chapter 7 - vascular imaging and radiation safety. In: Hallett JW, Mills JL, Earnshaw JJ, Reekers JA, Rooke TW, editors. Comprehensive vascular and endovascular surgery. second edition ed. Philadelphia: Mosby; 2009. p. 73–116. https://www.sciencedirect.com/science/article/pii/B978032305726400007X.
[51] Holzapfel GA, Gasser TC, Ogden RW. A new constitutive framework for arterial wall mechanics and a comparative study of material models. J Elast 2000;61:1–48.
[52] Bols J, Degroote J, Trachet B, Verhegghe B, Segers P, Vierendeels J. A computational method to assess the in vivo stresses and unloaded configuration of patient-specific blood vessels. J Comput Appl Math 2013;246:10–7.
[53] Ahamed T, Dorfmann L, Ogden R. Modelling of residually stressed materials with application to aaa. J Mech Behav Biomed Mater 2016;61:221–34.
[54] Pakeliani D, Van Herzeele I, Lachat ML, Vermassen FE. Evar 2020: training future aortic specialists, emerging need and the role of simulation. Endovasc Today 2017;16:95–7.